



# Recalibrating Gravitational Wave Phenomenological Waveform Model

KELVIN K. H. LAM,<sup>1</sup> KAZE W. K. WONG,<sup>2</sup> AND THOMAS D. P. EDWARDS<sup>3</sup>

<sup>1</sup>*Department of Physics, The Chinese University of Hong Kong, Shatin, N.T., Hong Kong*

<sup>2</sup>*Center for Computational Astrophysics, Flatiron Institute, New York, NY 10010, USA*

<sup>3</sup>*William H. Miller III Department of Physics and Astronomy, Johns Hopkins University, Baltimore, Maryland 21218, USA*

## ABSTRACT

We present a simple and general method of recalibrating gravitational wave (GW) phenomenological waveform models jointly. By using `jax` and `ripple`, we can perform automatic differentiation to functions, which allows us to use gradient-based optimization methods to recalibrate waveform coefficients in IMRPhenomD model. This method reduces systematic bias previously introduced to the model and generally can improve waveform accuracy. With recalibrated coefficients, we found that the typical *mismatch* has a 50% decrease. Furthermore, we analyze the accuracy base on the waveform's intrinsic parameters. We found that waveform accuracy has significant dependence on black hole spin. Reduced spin approximation introduces degeneracy in spin, which prevented further improvement. We isolated regions in the parameter space that does not fit the waveform ansatz. These results allow us to understand more about how to develop newer phenomenological models.

## 1. INTRODUCTION

In the future, the Laser Interferometer Gravitational-wave Observatory (LIGO) will finish its maintenance and start observing new gravitational wave (GW) results. This new O4 run is expected to double the rate of current binary black hole (BBH) observations (Abbott et al. 2020). Additionally, the sensitivity of interferometers will be increased to capture more details of GW. Having instruments with higher sensitivity, GW models of equal or higher accuracy than observations should be used to extract GW information. Otherwise, the extracted information would be affected more by GW models instead of interferometer sensitivity, resulting in a bottleneck in GW analyses. Although GW models are accurate enough for current analyses, the accuracy of current models will no longer suffice for future data analyses (Pürrer & Haster 2020). Hence, it is necessary for us to develop and improve GW models.

Currently, three families of GW models are commonly used. They are the effective-one-body (EOB) (Ossokine et al. 2020; Cotesta et al. 2020; Taracchini et al. 2014), Numerical Relativity (NR) surrogate (Islam et al. 2022; Varma et al. 2019b,a) and phenomenological (Phenom) models (Husa et al. 2016; Khan et al. 2016; García-Quirós et al. 2020; Pratten et al. 2021). EOB models

are constructed by mapping two masses onto an effective body under an effective metric; NR surrogate models construct waveforms using combinations of NR waveforms; Phenom models are formulated using specific ansatz and inspiral approximations. While EOB and NR surrogate models give better waveform approximants, Phenom waveforms can be produced much faster, hence it is used mostly in data analysis tasks that requires many waveform generations. This advantage scales up in data analysis tasks such as matched filtering and parameter estimation, where many waveforms are required in each run. This motivates us to improve upon the current framework of Phenom models, thus can retain the advantage of fast waveform generation while improving the model's accuracy.

Automatic differentiation (AD) is a method to calculate derivatives of functions up to machine precision. In traditional numerical calculations, derivatives are usually obtained through numerical derivatives. Symbolic derivatives were available but it was less efficient. Both methods were not viable in machine learning, where back-propagation requires precise and rapid derivative calculations. In `python`, packages including `pytorch` (Paszke et al. 2019), `tensorflow` (Abadi et al. 2015), etc. utilizes AD to train machine learning models. AD's algorithm is intuitive in nature. Functions defined are decomposed into tree structures of primitives, such as addition or function evaluations. Since these operations are fundamental, they were saved as pairs inter-

nally. Differentiation proceeds forward following the tree structure, with the application of the chain rule in each step to evaluate its derivative. Analytic derivatives of such operations are applied in each step and the desired derivative can then be obtained by composing back the original function according to the original structure. **ripple** (Edwards et al. 2023) was a new implementation of IMRPhenomD, one of the models within the Phenom family. It was first implemented in **lalsuite** using **C**. In order to make use of AD, it was rewritten using **jax**, a **python** package that supports AD. Using **ripple**, one can apply AD to GW models to obtain precise derivatives, thus allowing one to freely use derivative-based algorithms to perform data analyses.

In this paper, we investigate the possibility of further improving the accuracy of IMRPhenomD by jointly optimizing all the fitting coefficients given NR waveforms, and what constraints one may face when trying to further improve. We find that simply by applying gradient descent algorithm, one can obtain a better set of waveform coefficients, thus improving the accuracy of the model. Furthermore, by comparing the accuracy of optimized and original waveforms, we find that model-generated waveforms are very sensitive to their intrinsic parameters. Specifically, IMRPhenomD favors certain parts of the parameter space. This means IMRPhenomD introduces systematic bias to other GW analysis tasks. This showcases the flaws of the ansatz and allows us to have a deeper understanding of Phenom models.

The rest of the paper is structured as follows: In Sec. 2, we review the parameterization of the IMRPhenomD model and the mismatch function that is used as an objective function for the calibration, followed by outlining the specific optimization scheme used for recalibration. In Sec. 3, we give the optimization result by comparing mismatches of optimized waveforms with original waveforms. We also show how the optimization result differs with waveforms of different intrinsic parameters. In Sec. 4, we address the difference between our calibrating procedure with (Khan et al. 2016). We also explain how reduced spin parameterization affects the accuracy of the model.

## 2. METHOD

### 2.1. Waveform Model

In order to recalibrate the model, we have to understand what parameters the model has. Here we give a succinct summary of the IMRPhenomD model and the relevant parameters. For interested readers, please refer to (Khan et al. 2016) for more details on construction of the model.

The IMRPhenomD model is constructed by combining three individually fitted parts into one coherent waveform model, which consists of the inspiral, intermediate, and merger-ringdown part,

$$h(f, \theta, \Lambda^i) = h_{\text{ins}}(f, \theta, \Lambda^i) + h_{\text{int}}(f, \theta, \Lambda^i) + h_{\text{rd}}(f, \theta, \Lambda^i). \quad (1)$$

Instead of fitting the strain, which is a highly oscillatory function that is difficult to fit, the amplitude and phase are fitted since they are smoother functions. In each part, the amplitude and phase are made using simple functions of frequency such as polynomials or lorentzians. Specifically, the merger-ringdown amplitude is fitted by a lorentzian and the other parts are fitted using polynomials.

$$\begin{aligned} A_0 &\equiv \sqrt{\frac{2\eta}{3\pi^{1/3}}} f^{-7/6} \\ A_{\text{ins}}(f; \theta) &= A_{\text{PN}}(f; \theta) + A_0 \sum_{i=1}^3 \rho_i f^{(6+i)/3} \\ A_{\text{int}}(f; \theta) &= A_0 (\delta_0 + \delta_1 f + \delta_2 f^2 + \delta_3 f^3 + \delta_4 f^4) \\ A_{\text{rd}}(f; \theta) &= A_0 \left[ \gamma_1 \frac{\gamma_3 f_{\text{damp}}}{(f - f_{\text{RD}})^2 + (\gamma_3 f_{\text{damp}})^2} e^{-\frac{\gamma_2 (f - f_{\text{RD}})}{\gamma_3 f_{\text{damp}}}} \right], \end{aligned} \quad (2)$$

where  $A_{\text{PN}}$  is the post-newtonian expansion of the inspiral amplitude up to order  $A_0 f^2$ ,  $f_{\text{damp}}$  is the damping frequency, and  $f_{\text{RD}}$  is the frequency at ringdown. The ansatzes for phase can be found in (Khan et al. 2016). These simple analytic functions consists of parameters  $\Lambda^i = \{\rho_i, \delta_i, \gamma_i\}$ , which are defined as follows.

$$\begin{aligned} \Lambda^i &= \lambda_{00}^i + \lambda_{10}^i \eta \\ &+ (\chi_{\text{PN}} - 1)(\lambda_{01}^i + \lambda_{11}^i \eta + \lambda_{21}^i \eta^2) \\ &+ (\chi_{\text{PN}} - 1)^2(\lambda_{02}^i + \lambda_{12}^i \eta + \lambda_{22}^i \eta^2) \\ &+ (\chi_{\text{PN}} - 1)^3(\lambda_{03}^i + \lambda_{13}^i \eta + \lambda_{23}^i \eta^2), \end{aligned} \quad (3)$$

where  $\lambda$  are fitting coefficients obtained during calibration,  $\eta$  is the symmetric mass ratio, and  $\chi_{\text{PN}}$  is the post-Newtonian spin parameter, which is defined as

$$\chi_{\text{PN}} = \frac{m_1 \chi_1 + m_2 \chi_2}{m_1 + m_2} - \frac{38\eta}{113} (\chi_1 + \chi_2). \quad (4)$$

Here,  $m_{1,2}$  and  $\chi_{1,2}$  are the primary and secondary mass and spin, respectively. Finally, the individual segments are first connected directly using step functions. Then, by fixing coefficients in the intermediate segment, one can make the final waveform is continuous in its first derivative.

Combining Eq. 1, 2 and 3, we can see that the entire waveform is non-linear in  $\lambda$ . A slightly inaccurate set

of  $\lambda$  can significantly affect the shape of the generated waveforms. Thus, having a set of accurate waveform coefficients is important and fundamental to having accurate GW models. Generally, waveform coefficients are obtained by calibrating with NR waveforms, which are waveforms computed using NR simulations. In the case of (Khan et al. 2016), they first obtain a set of  $\Lambda$  by fitting model generated waveforms to Eq. 2 and the phase ansatzes. Repeating with different NR waveforms, they obtain multiple sets of  $\Lambda$ , and  $\lambda$  are subsequently found by fitting against Eq. 3. Since the fitting procedure is done in a piece-wise manner, the correlations between different segments are omitted, which could limit the accuracy of the model. Also, since fitting was performed before connecting individual segments, the final waveform does not guarantee to achieve the optimal waveform. The connecting procedure alters the previously fitted waveform. Hence, the model generated waveforms contains additional inaccuracies.

Instead, we recalibrate coefficients jointly, which we can remove inaccuracies and biases discussed above, and can improve model accuracy. In the past, due to the complex nature of GW strains and piece-wise formalism of IMRPhenomD, non-linear fitting was difficult to be performed in optimizing coefficients. Hence, piece-wise optimization was done to obtain coefficients. However, with `ripple` and AD from `jax`, gradients of IMRPhenomD can be easily obtained, thus allowing the use of gradient-based algorithms for us to recalibrate the model.

## 2.2. Loss Function

In order to recalibrate the model, we need to define an objective function that quantify the performance of the model. A common choice for such metric is the *mismatch* function (Husa et al. 2016). It is defined as

$$\mathcal{M}(h_1, h_2) = 1 - \max_{t_0, \phi_0} \langle \hat{h}_1, \hat{h}_2 \rangle, \quad (5)$$

where  $h_{1,2}$  are the two GW waveform we are comparing, and  $t_0$  and  $\phi_0$  are time shift and phase shift respectively. The  $\langle h_1, h_2 \rangle$  is commonly referred as the inner product, which is defined as

$$\langle h_1, h_2 \rangle = 4 \operatorname{Re} \int_{f_{\min}}^{f_{\max}} \frac{h_1(f) h_2^*(f)}{S_n(f)} df, \quad (6)$$

where  $\hat{h} = h/\sqrt{\langle h, h \rangle}$  is the normalized GW strain,  $S_n(f)$  is the power spectral density(PSD) of noise from the instrument,  $f_{\max}$  and  $f_{\min}$  are the relevant maximum and minimum frequencies for the integration.  $t_0$  and  $\phi_0$  are maximized by performing regression between  $h_1$  and  $h_2$ . The mismatch is a quantity that is closely

related to the mean square error (MSE) between the two waveforms, as it is often considered a weighted version of the MSE.

Since we wish to optimize the model over the whole parameter space, we need to compare multiple model generated waveforms with NR waveforms. However, mismatch only quantifies the difference between IMRPhenomD and NR waveform for one particular set of intrinsic parameters. To take into account of various different waveforms in the parameter space, we pick waveforms from the different parts of the parameter space. We define the loss function as an average of training waveforms in two ways, the simple average of mismatches and the normalize average of mismatches,

$$\mathcal{L}_{\text{mean}} = \frac{1}{N} \sum_{i=1}^N \mathcal{M}_i \quad (7)$$

$$\mathcal{L}_{\text{fl}} = \frac{1}{N} \sum_{i=1}^N \frac{\mathcal{M}_i}{\mathcal{M}_{i,\text{ini}}}, \quad (8)$$

where  $\mathcal{M}_i$  represents the mismatch of an individual training waveform,  $\mathcal{M}_{i,\text{ini}}$  represents the initial mismatch of the individual training waveform, and  $N$  is the total number of individual training waveforms. Note that we choose to use two different averages, since they have different preferences in optimization base on waveform mismatches. For the first choice, simple average serves as the simplest choice of loss function, but is prone to be dominated by a single waveform with a large mismatch. Other waveforms with smaller mismatches would be insignificant comparatively, and might not be able to improve under such optimization. Alternatively, the second choice, normalized average eliminates the aforementioned issue. Nevertheless, it excludes the information on initial mismatches.  $\mathcal{L}_{\text{fl}}$  restricts every training waveform to decrease at similar rates, hence it is hard to obtain optimized waveforms with mismatches in the same order of magnitude. Instead, their ratios in mismatches would remain approximately the same. Conversely,  $\mathcal{L}_{\text{mean}}$  allows the loss function to automatically adjust and individual mismatches would be in a similar order of magnitude after optimization. In this paper, we showcase the results of using both loss functions and examine the differences between them.

## 2.3. Optimization Scheme

To compute the loss functions, we have to take NR waveforms for calculating the mismatch. We choose 11-16 NR waveforms from the set of waveforms used in the original calibration process as training waveforms. Originally, 19 waveforms are taken from NR simulations for calibrating IMRPhenomD (Khan et al. 2016), which are

waveforms from the SXS catalog (Boyle et al. 2019) or BAM simulation. As BAM waveforms are not publicly available, we cannot take the identical training set as them. Instead, we take the available waveforms from the SXS catalog to construct our loss function. Training waveforms used are listed in Tab. 1 and 2. The training waveforms chosen has maximum mass ratio to be 8. This is because SXS catalog does not have NR waveforms with extremely high mass ratio. In fact, the SXS catalog only has NR waveforms with  $q \leq 10$ . Nevertheless, we are interested in the behavior of IMRPhenomD model with small  $q$ , as most BBH events observed from LIGO have  $q \leq 8$ . Hence, we calibrate IMRPhenomD with waveforms of  $q \leq 8$ .

In the SXS catalog, NR waveforms are in the form of time-series strain. Since time-series data is oscillatory, performing optimization in the time-domain is not ideal. Hence, we transform NR waveforms to frequency-domain to compare with IMRPhenomD waveforms with the same intrinsic parameters. We taper the time-series using Tukey window.<sup>1</sup> Then, the frequency spectra can be obtained by taking the Fourier transform of the time-series.

Other than NR waveforms, one need to choose a relevant noise PSD for mismatch. We have opted to use a flat PSD for this purpose, as it provides results that are independent of the detector sensitivity and mass scale. The use of a flat PSD ensures that the improvement in accuracy is due mainly to the difference in high-dimensional fitting and piece-wise fitting, but not due to the use of a different mass scale. Furthermore, we are interested in examining the effect of introducing a detector PSD on the optimization process. For this, we have chosen the zero-detuned high-power (zdethp) noise PSD (Aasi et al. 2015). Since the total mass of the system scales with the frequency of the waveform, we must choose a corresponding mass scale to match the frequency range of our noise PSD. We selected an arbitrary mass scale of  $M = 50M_\odot$  for all waveforms for demonstration, as this is a commonly observed mass scale in LIGO observations.

We point out that our treatment to NR waveforms is different from that of (Husa et al. 2016; Khan et al. 2016). In the original calibration process, training waveforms are hybrid waveforms of NR and SpinAlignedEOB (SEOBO) waveforms. The low frequency inspiral part is taken from the SEOBO waveforms while the rest of the waveforms are taken from NR simulations. Instead, we

<sup>1</sup> Specifically, we choose  $\alpha = 2t_{\text{RD}}/T$ , where  $t_{\text{RD}}$  is the duration of ringdown and  $T$  is the duration of the entire GW strain.

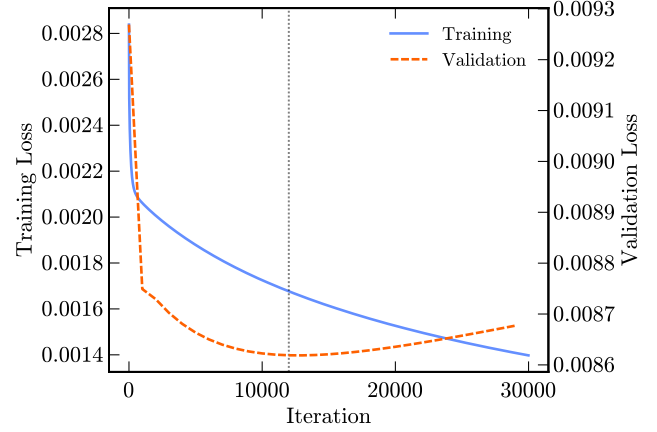


**Figure 1.** The value of loss function Loss functions against number of iterations. The code is terminated after 30000 steps. We take the set of coefficients at the minimum of the validation loss.

solely use NR waveforms for comparison, since we are only exploring the possibility of optimizing waveform models. Thus, for simplicity sake, we ignore this procedure. On the other hand, most NR waveforms used (for both training and testing) have long enough time series data, i.e.  $> 15$  orbits (Boyle et al. 2019), in which they are long enough to contain part of the inspiral segment and all merger and ringdown frequency information. We take the frequency limits as  $f_{\text{min}} = 0.1f_{\text{RD}}$  and  $f_{\text{max}} = 1.2f_{\text{RD}}$ , where  $f_{\text{RD}}$  is the frequency at ringdown. This range covers most of the IMRPhenomD's frequency range, except the minimum frequency is set higher than that in the original calibration due to NR length. When compared with IMRPhenomC, the frequency range is slightly extended to have a higher maximum frequency. We have the dimensionless frequency spacing  $M\Delta f = 2.5 \times 10^{-6}$ , which is sufficient to capture all features of GW strain.

With the loss function evaluated, we apply gradient descent to optimize the tunable coefficients as shown in Algorithm 1. We take  $\lambda_i$  to be the original coefficients given in (Khan et al. 2016). We take them as the initial waveform coefficients because they lie in the neighborhood of the minimum that we wish to find. Then, by taking  $\alpha = 10^{-6}$ , we see the validation loss in Fig. 1 plateau at around  $N = 30000$   $N = 12000$ , hence we end the optimization here.

### 3. RESULT AND COMPARISON WITH ORIGINAL MODEL

To evaluate the effectiveness of the optimization, we analyze approximately 530 NR waveforms 536 NR waveforms from the SXS catalog in this study. We specifically select waveforms with negligible eccentricity ( $e < 2 \times 10^{-3}$ ) and precession

**Algorithm 1:** Gradient descent pseudocode

---

**Input:** initial coefficients  $\lambda_i$   
**Parameters:** number of iterations  $N$ , learning rate  $\alpha$   
**Variables:** current coefficients  $\lambda$ , mismatch gradient  $\nabla \mathcal{L}$   
**Result:** output coefficients  $\lambda$

```

1  $\lambda \leftarrow \lambda_i$ 
/* Gradient Descent */
2 for  $i < N$  do
3    $\mathcal{L} \leftarrow \text{Mismatch}(\lambda)$ 
4    $\nabla \mathcal{L} \leftarrow \text{AutoDiff}(\mathcal{L})$ 
5    $\lambda \leftarrow \lambda - \alpha \nabla \mathcal{L}$ 
6 return  $\lambda$ 

```

---

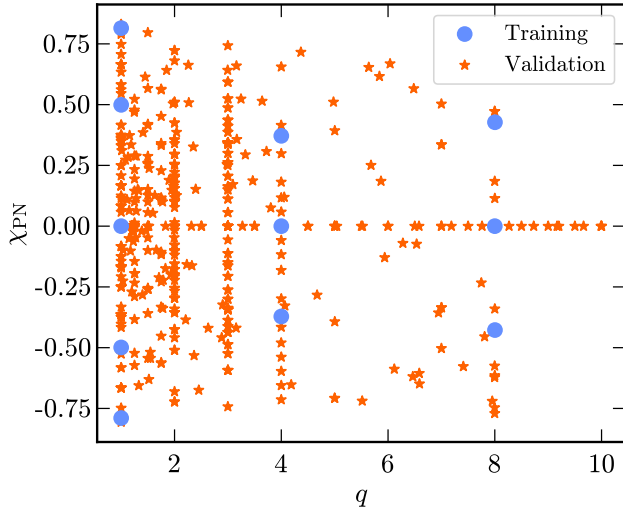


**Figure 2.** Parameter space with mass ratio  $q$  against normalized reduced post-newtonian spin parameter  $\chi_{\text{PN}}$ . Orange: Training waveforms; Blue: Testing waveforms

( $\chi_{x,y} < 5 \times 10^{-3}$   $\chi_{x,y} < 5 \times 10^{-3}$ ) that are consistent with the constraints of the waveform model. As shown in Fig. 2, the intrinsic parameters of the chosen test waveforms fall within the parameter space defined by the training waveforms. This suggests that these test waveforms can be used for direct comparison with the original model.

To illustrate the improvement on an individual waveform level, we compare a particular waveform before and after optimization in Fig. 3. Compared to the original IMRPhenomD waveform, we can see the optimized waveform has smaller residual from NR waveform both in amplitude and phase, particularly in the inspiral region, where the amplitude displays a 50% reduction in error. For a fair comparison, we selected one of the testing waveforms from the catalog presented in (Khan et al. 2016).

Code	$q$	$\chi_1$	$\chi_2$
SXS:BBH:0156	1.0	-0.95	-0.95
SXS:BBH:0151	1.0	-0.60	-0.60
SXS:BBH:0001	1.0	0.00	0.00
SXS:BBH:0152	1.0	0.60	0.60
SXS:BBH:0172	1.0	0.98	0.98
SXS:BBH:1418	4.0	-0.40	-0.50
SXS:BBH:0167	4.0	0.00	0.00
SXS:BBH:1417	4.0	0.40	0.50
SXS:BBH:0064	8.0	-0.50	-0.46
SXS:BBH:0063	8.0	0.00	0.00
SXS:BBH:0065	8.0	0.50	0.46

**Table 1.** List of waveforms used to recalibrate the model. The mass ratio  $q = m_1/m_2 \geq 1$  with spins  $\chi_{1,2}$ . Out of the 11 waveforms listed here, 9 of them are also used in the original IMRPhenomD calibration. (Khan et al. 2016) The two remaining waveforms were from BAM simulation, to which we do not have access.

Code	$q$	$\chi_1$	$\chi_2$
SXS:BBH:0234	2.0	-0.85	-0.85
SXS:BBH:0235	2.0	-0.60	-0.60
SXS:BBH:0169	2.0	0.00	0.00
SXS:BBH:0256	2.0	0.60	0.60
SXS:BBH:0257	2.0	0.85	0.85

**Table 2.** Additional waveforms used in further recalibration.

To quantify the effect of optimization over the entire dataset, We evaluate the mismatch of all testing waveforms using a constant PSD weighted loss function,  $\mathcal{L}_{\text{mean}}$ . We present the resulting distribution in Fig. 4. The peak of the distribution has shifted towards a lower mismatch, with a decrease of almost one order of magnitude and a 50% reduction in the median. When using  $\mathcal{L}_{\text{fl}}$ , we observe a similar improvement with a 22.9% decrease in the median. Even though the distribution lacks a clear peak due to the problem discussed in Section 2.3, both distributions show observable improvement, and the optimization scheme remains unaffected.

Applying the same methods, we observe will see that the distributions of mismatches calculated using the **zdetph** PSD exhibit superior improvement compared to the weighted mismatch unweighted mismatch. The shape of the distribution is similar to that shown in Fig. 4. This result is expected, as the IMRPhenomD model was initially constructed and fitted using the **zdetph** weighted mismatch. Consequently, the model is anticipated to



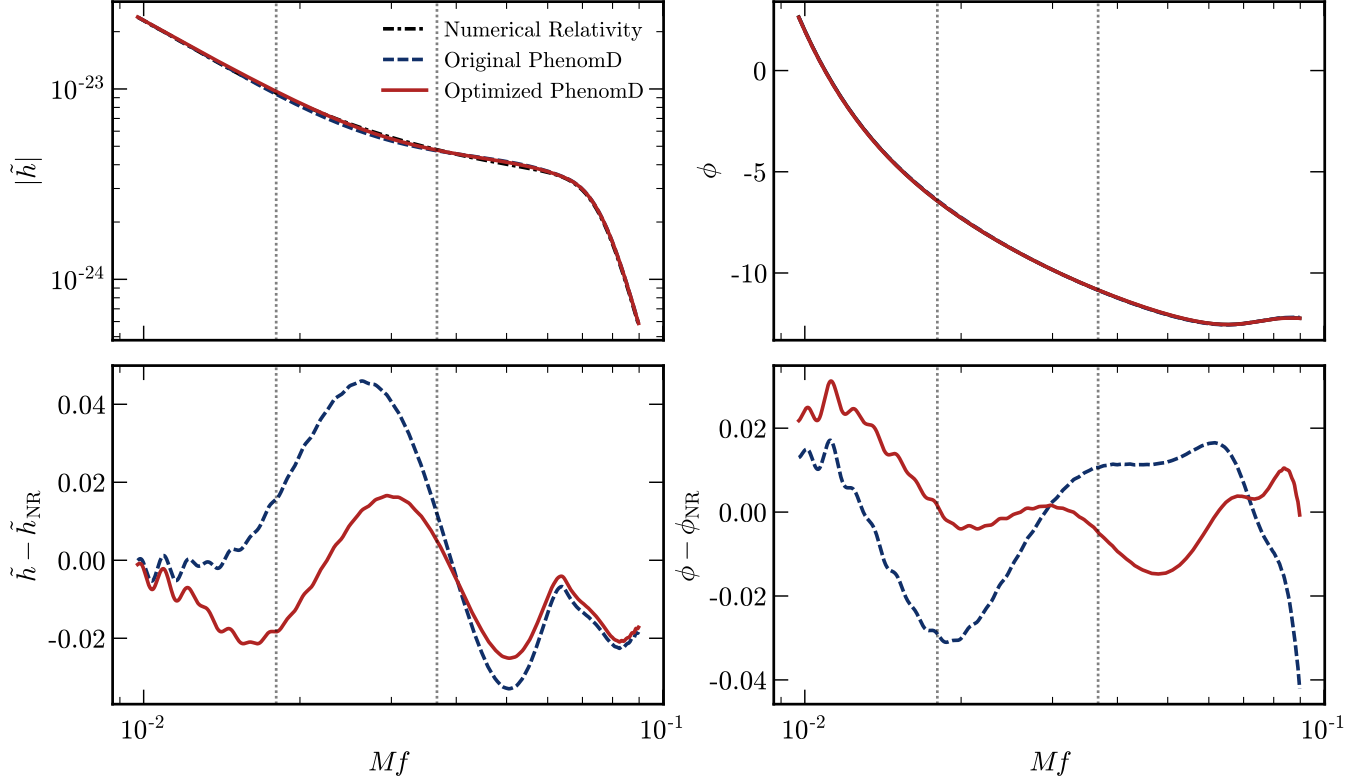


**Figure 3.** Comparison between original and optimized IMRPhenomD waveforms. Here shows the SXS:BBH:0154 NR waveform, which has mass ratio  $q = 1$  and  $\chi_1 = \chi_2 = -0.8$ . The original mismatch is around  $2.8 \times 10^{-4}$  and the optimized mismatch is around  $5.3 \times 10^{-5}$ . Top: It shows the amplitude and phase of NR, original IMRPhenomD and optimized IMRPhenomD waveform. Bottom: It shows the relative error of amplitudes between NR and IMRPhenomD waveforms, and the absolute error of phases between NR and IMRPhenomD waveforms

closely fit the NR waveforms while incorporating the influence of the `zdetph` PSD, rather than a constant PSD.

Motivated by the successful improvement of the waveforms, we expand the training dataset to optimize additional waveforms listed in Tab. 2. . We specifically choose to use  $q = 2$  events since we have abundant  $q = 2$  NR waveforms to validate the final result. The new set of coefficients generated from this optimization process yields only marginal improvements in the newly produced waveforms, as seen in Fig. 5. The high mismatch tail of the optimized distribution remains comparable in length and endpoint to the original distribution, indicating that our procedure is incapable of improving these waveforms. Similarly, utilizing the `zdetph` PSD to optimize the loss function with additional waveforms leads to similar improvement in the resulting distribution.

Although most of the waveforms show improvement in figure 4, the high mismatch tail of the distribution remains unaffected. Given that the waveform model’s ansatz may not be entirely compatible with NR, and the optimization procedure is carried out over a distribution of waveforms with varying intrinsic parameters, it is conceivable that some trade-offs in accuracy exist

between different parts of the parameter space. If this is the cause of the lack of improvement in the high mismatch tail of the distribution, segmenting the parameter space into smaller subspaces should alleviate this problem. On the other hand, if the ansatz lacks the correct parameterized form to capture the NR waveforms’ behavior as a function of the intrinsic parameters, the results will always be biased, and we should not expect any improvement, even if we segment the parameter space during training.

Since we know intrinsic parameters play an important role in the ansatz, we would like to investigate how intrinsic parameters affect the recalibration process. First, we plot the parameter space of  $q$  vs.  $\chi_{PN}$  in Fig. 6. We can see near non-spinning waveforms demonstrate more consistent improvement, since the ansatz are developed base on non-spinning waveforms. Also, the original coefficients were fitted using NR waveforms with equal or similar spin, hence the model prefers waveforms with similar spin. On the other hand, spinning waveforms can either improve or worsen in terms of mismatch base on their intrinsic parameters. To further discuss the behavior of non-spinning waveforms, we plot the param-

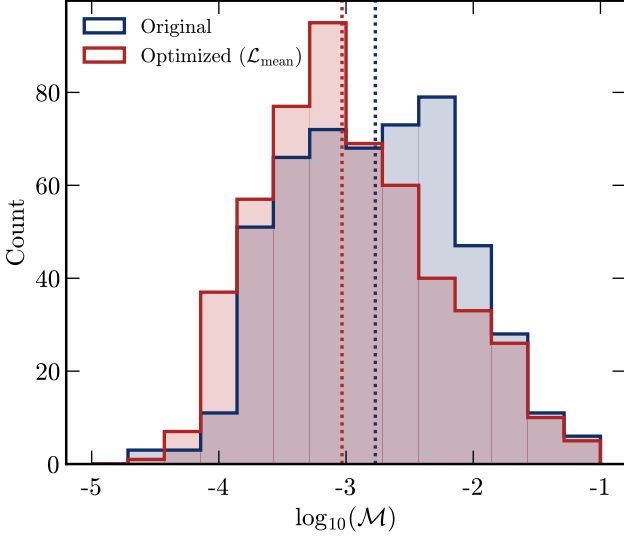


**Figure 4.** Distributions of waveform mismatches calculated using both  $\mathcal{L}_{\text{mean}}$  and  $\mathcal{L}_{\text{fl}}$ . We use training waveforms listed in Tab. 1 and mismatches are weighted with the constant PSD. For the  $\mathcal{L}_{\text{mean}}$  distributions, the median (dashed blue lines) decreased by 50.0% while represent the median of  $\mathcal{L}_{\text{fl}}$  distribution the distributions, which has decreased by 22.945.3%.

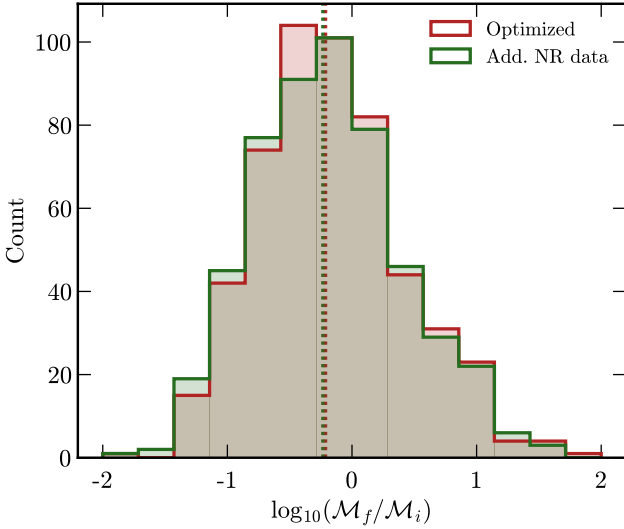


**Figure 5.** Distributions of  $\log_{10}$  difference in mismatch. The distribution labeled q148 uses training waveforms listed in Tab. 1 while the q1248 distribution uses waveforms listed in Tab. 1 and 2. Mismatches are calculated using the constant PSD with the loss function  $\mathcal{L}_{\text{mean}}$ . Dashed lines represent the median of the distributions, which has decreased by 10.4%.

ter space of  $\chi_1$  vs.  $\chi_2$  in Fig. 7. Waveforms along the diagonal axis, i.e.  $\chi_1 \approx \chi_2$ , show good mismatch improvements as discussed above. Meanwhile, the top-left ( $\chi_1 < 0$  and  $\chi_2 > 0$ ) and bottom-right ( $\chi_1 > 0$  and  $\chi_2 < 0$ ) regions respond to optimiza-

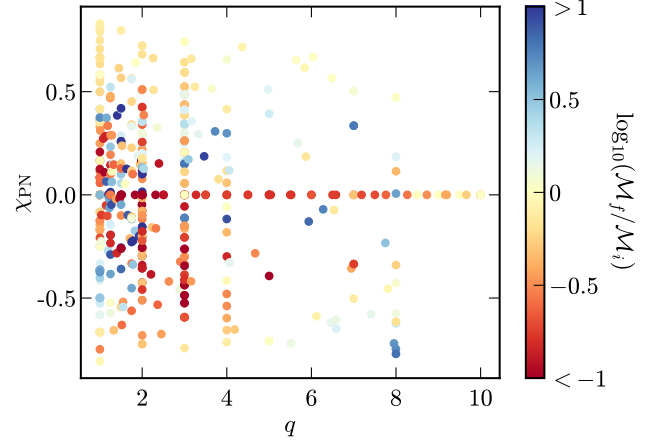


**Figure 6.** Parameter space of testing waveforms of with  $q$  vs. against  $\chi_{\text{PN}}$ . We use show the recalibrated result from optimizing  $\mathcal{L}_{\text{mean}}$  with the constant noise spectrum PSD and training waveforms in Tab. 1. Here, the colorbar represents the  $\log_{10}$  difference between optimized and original unweighted mismatches.

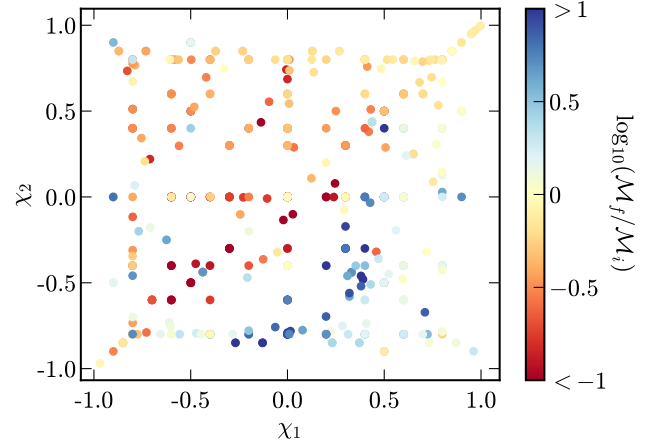


**Figure 7.** Parameter space of testing waveforms of with  $\chi_1$  vs. against  $\chi_2$ . We use show the recalibrated result from optimizing  $\mathcal{L}_{\text{mean}}$  with the constant noise spectrum PSD and training waveforms listed in Tab. 1.

tion differently. In the top-left region, waveforms generally improve slightly with along optimization. However, mismatches waveforms in the bottom-right region do not improve after optimization. Most Some waveforms even turned worse after optimization.

We divided the parameter space into four regions to analyze the effect of the recalibration procedure on each region separately (Fig. 79). The training waveforms used for fitting are listed in TableTab. 3. The top-left and bottom-right regions have limited data for  $q > 4$ , hence the results are only valid up to  $q \lesssim 4$ . From Fig. 9, we observe improvements in waveform mismatch for all

Code	$q$	$\chi_1$	$\chi_2$
SXS:BBH:0172	1.0	0.98	0.98
SXS:BBH:0152	1.0	0.60	0.60
SXS:BBH:0001	1.0	0.00	0.00
SXS:BBH:1417	4.0	0.40	0.50
SXS:BBH:0167	4.0	0.00	0.00
SXS:BBH:1426	8.0	0.48	0.75
SXS:BBH:0167 0063	8.0	0.00	0.00
<hr/>			
SXS:BBH:0370	1.0	-0.20	0.40
SXS:BBH:2092	1.0	-0.50	0.50
SXS:BBH:0330	1.0	-0.80	0.80
SXS:BBH:2116	2.0	-0.30	0.30
SXS:BBH:2111	2.0	-0.60	0.60
SXS:BBH:0335	2.0	-0.80	0.80
SXS:BBH:0263	3.0	-0.60	0.60
SXS:BBH:2133	3.0	-0.73	0.85
SXS:BBH:0263	4.0	-0.80	0.80
<hr/>			
SXS:BBH:0156	1.0	-0.95	-0.95
SXS:BBH:0151	1.0	-0.60	-0.60
SXS:BBH:0001	1.0	0.00	0.00
SXS:BBH:1418	4.0	-0.40	-0.50
SXS:BBH:0167	4.0	0.00	0.00
SXS:BBH:1419	8.0	-0.80	-0.80
SXS:BBH:0063	8.0	0.00	0.00
<hr/>			
SXS:BBH:0304	1.0	0.50	-0.50
SXS:BBH:0327	1.0	0.80	-0.80
SXS:BBH:2123	2.0	0.30	-0.30
SXS:BBH:2128	2.0	0.60	-0.60
SXS:BBH:2132	2.0	0.87	-0.85
SXS:BBH:2153	3.0	0.30	-0.30
SXS:BBH:0045	3.0	0.50	-0.50
SXS:BBH:0292	3.0	0.73	-0.85

**Table 3.** List of waveforms used in recalibrating coefficients in 4 regions. From top to down are the top-right ( $\chi_1, \chi_2 > 0$ ), top-left ( $\chi_1 < 0 < \chi_2$ ), bottom-left ( $\chi_1, \chi_2 < 0$ ) and bottom-right ( $\chi_1 > 0 > \chi_2$ ) regions. Note that for the top-right and bottom-left regions, waveforms are chosen to have **equal or similar spins**  $\chi_1 \approx \chi_2$ , while the training waveforms for the other two regions are chosen to have **opposite spins**  $\chi_1 \approx -\chi_2$ .

waveforms, except those in the bottom-right region. For **that** equal-spin waveforms lying in the proximity of the diagonal axis, the mismatch has additional improvement due to most training waveforms being equal-spin. In the top-left region **on the diagonal has great improvement**. Above the diagonal, the improvement is significant, except for a few defects caused by some testing waveforms having  $q > 4$ . This can be seen clearer in Fig. 8, which we see that the optimized histogram

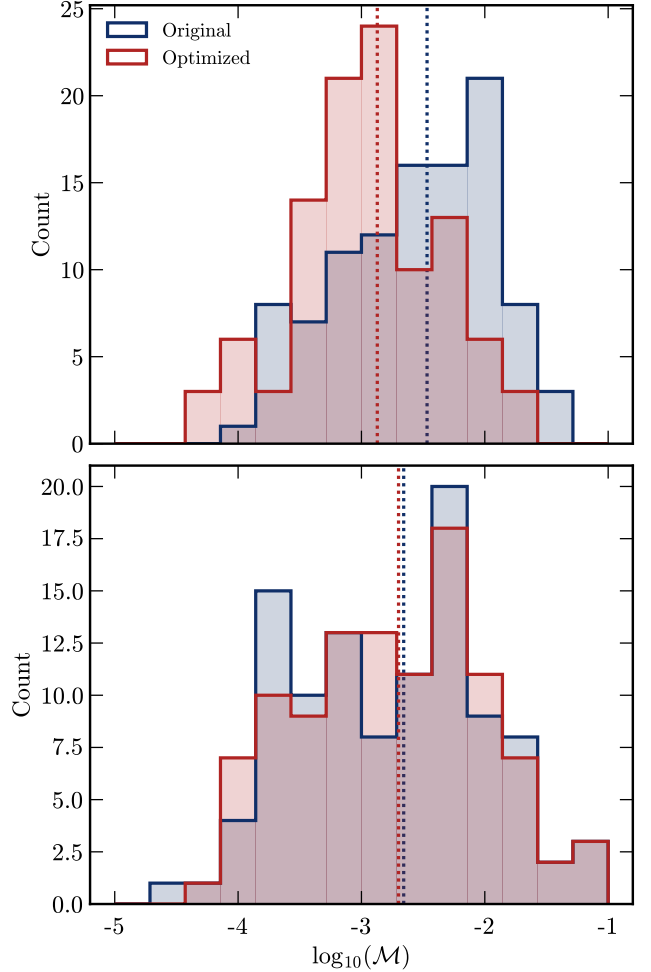


**Figure 8.** Distributions of mismatches in the top-left (Top) and bottom-right (Bottom) regions. We use a constant noise spectrum to calculate mismatch and  $\mathcal{L}_{\text{mean}}$  for as the loss function. Waveforms in the top-left region generally improves while waveforms in the bottom-right region **worsened** **has very little improvement**, as indicated by the median (dashed lines).

shifts downward uniformly. **The optimized waveforms in the Below the diagonal, waveforms have negligible improvement** (Fig. 8 and 9), indicating the original set of coefficients is the optimal set of coefficients, and cannot be further improved. Hence, we can deduce IMRPhenomD has better match with the top-left region and does not fit well with waveforms lying in the bottom-right region have a higher mismatch than the original ones, indicating poor fitting. These waveforms correspond to the waveforms in the high mismatch tail in Fig. 4, which we can see in Fig. 8. Thus, we show that further optimization region. Thus, the ansatz restricts additional improvements and further optimizing in a smaller subspace **does not region does not generally improve the results**.

#### 4. DISCUSSION



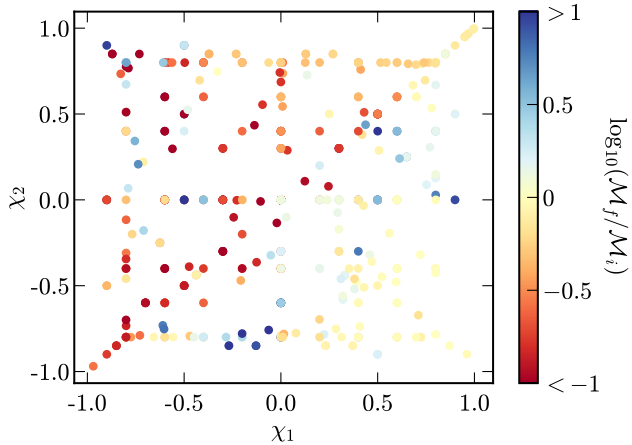


**Figure 9.** Parameter space of testing waveforms. Each region is fitted independently with waveforms listed in Tab. Colorbar represents log difference of mismatches before and after optimization 3.

We have shown the result of recalibrating waveform coefficients. One thing to note is that our recalibration procedure is not exactly the same as the original calibration. For instance, we use a different set of NR waveforms, frequency range, etc. Nonetheless, as the decrease in mismatch is rather significant, this optimization procedure should be able to improve the accuracy of IMRPhenomD on a similar scale regardless of the differences. Here, this the result serves as a demonstration of the general method used.

The results presented in Fig. 5 demonstrate that increasing the number of training waveforms used in waveform optimization yields only a marginal increase in accuracy. Our analysis suggests that this marginal improvement is a consequence of over-determination of the waveform coefficients. Consequently, increasing the number of calibration NR waveforms is unlikely to result in any significant improvement of the model’s accuracy. These observations suggest that the parameterized ansatz employed in our study may not be suitable for certain regions in the parameter space, leading to low mismatches for some waveforms while other waveforms remain at the high mismatch tail with negligible changes. This highlights the constraints of the model’s flexibility that ultimately limit its performance.

The reduced spin approximation is a major contributor to the inaccuracies observed in the ansatz. In IMRPhenomD, this approximation employs a single spin parameter,  $\chi_{\text{PN}}$ , as described in Sec. 2. The parameterization of BBH mergers using a single spin parameter results in a degeneracy within the parameter space. Specifically, black hole events with different spins may

generate the same waveform due to identical values of  $\chi_{\text{PN}}$ , leading to erroneous results, particularly for highly unequal spin events. This degeneracy produces straight lines in the parameter space with negative slopes that depend on the mass ratio, as shown which can be seen in Fig. 7. Notably, the ansatz performs better in the top left top-left region than the bottom right along a degeneracy line bottom-right region. In an attempt to address this issue, we partitioned the parameter space into four regions, as described in Sec.3. However, even with 3. With separate optimizations for each regions, Fig. 9 indicates that the bottom-right region exhibits similar mismatches as before, while the top-left region’s performance has improved, while the bottom-right region hardly improves. This observation suggests that the ansatz is specific to certain regions of the parameter space, with a preference for BBH events featuring  $\chi_1 < 0$  and  $\chi_2 > 0$  lying above the diagonal, and it has limited enhancement for events lying below the diagonal.

The division of the parameter space into four regions was a simple approach taken for practical reasons. A more systematic approach would involve the use of level set estimation algorithms to identify regions of interest within the parameter space. Such an algorithm can reveal additional degeneracies or issues that may exist within the ansatz. One possible strategy is to recalibrate individual regions of interest to achieve better results. An alternative approach is to select regions based on degeneracy lines. However, due to the limited number of NR waveforms available, we were unable to implement this approach. With more NR waveforms available in the future that cover the entire parameter space, we can perform optimization with fewer restrictions and select regions more systematically. Other than how to divide regions of interest, the choice of training waveforms also affects the final results greatly. Note that the choice of training waveforms listed in Tab. 3 were taken arbitrarily to test the effectiveness of separate fitting. Hence, if one takes a different set of training waveforms over the parameter space, the result might give additional features that can test and explain IMRPhenomD better.

Although our study primarily focused on the IMRPhenomD model, this simple yet versatile approach can be applied to other differentiable GW models, such as the IMRPhenomP (Hannam et al. 2014) or IMRPhenomX (Pratten et al. 2020) (Hannam et al. 2014; ?) or IMRPhenomX (Pratten et al. 2020, 2021) models within the same family. By jointly optimizing a new set of coefficients, it is expected that both models can be enhanced since they share similar construction principles to the IMRPhenomD model. For instance, they also use PN approximants as part of the ansatz in the inspiral segment. It will be in-

interesting to recalibrate the **IMRPhenomX** **IMRPhenomXAS** model (Pratten et al. 2020). Because it is parameterized by an additional anti-symmetric spin parameter, it is expected not to exhibit the degeneracy previously described. **With the currently developing jax IMRPhenomXAS model in ripple**, A more detailed investigation may provide valuable insights into the systematics of the Phenom models. Furthermore, this approach is applicable to other GW model families, such as NR surrogate models or EOB models introduced **previously. in Sec. 1.** Such an approach could simplify NR waveform calibration procedures and lead to the improvement of existing models.

## 5. CONCLUSION

In this paper, we have presented a systematic method to recalibrate GW models. This method utilizes **jax**'s automatic differentiation to apply derivative-based optimization to recalibrate GW models jointly. Using the new implementation of the IMRPhenomD model, **ripple**, which is written in **jax**, in conjunction with NR waveforms from the SXS catalog, we recalibrate waveform coefficients of the IMRPhenomD model. In general, the waveform accuracy can be improved by 50%. Comparing **zdehp** weighted and unweighted mismatch, weighted mismatches have a slightly better improvement. In contrast, different types of loss function result in significantly different final mismatch distributions. As seen in Fig. 4,  $\mathcal{L}_{\text{mean}}$  outperforms  $\mathcal{L}_{\text{fit}}$   $\mathcal{L}_{\text{fl}}$ . By increasing the number of training waveforms, we see a slight improvement increase in Fig. 5.

Furthermore, we investigated how the intrinsic parameters affect the improvement. Fig. 7 shows that the optimization procedure has a certain preference for waveforms lying in the top-left region while the bottom-right region **cannot be hardly** improved. To further test this result, we recalibrate waveforms in separate regions in parameter space. From Fig. 9, we can see that this recalibration process gives further improvement to the top-left region while the bottom-right region **shows similar result only have little improvement**. This indicates that the ansatz **has limited match in this region and** does not fit **most** waveforms in this region, **hence introduces bias to downstream GW analysis**. This phenomenon is **mainly** due to the reduced spin approximation used in parameterizing the ansatz, where degeneracies between  $\chi_1$  and  $\chi_2$  are introduced.

While we naively separate the optimization process into 4 regions, one can perform systematic region-selection. In principle, we can apply this general method to other newer and more accurate models such as IMRPhenomX or IMRPhenomP models. Then, we can perform all the above analyses to understand how to construct better GW Phenom models in the future.

## 6. ACKNOWLEDGMENTS

We thank Will M. Farr, Max Isi, and Mark Hannam for helpful discussions; we also thank Carl-Johan Haster, Neil J. Cornish and Thomas Dent for comments on the draft. The Flatiron Institute is a division of the Simons Foundation. T.E. is supported by the Horizon Postdoctoral Fellowship.

## REFERENCES

- Aasi, J., Abbott, B., Abbott, R., et al. 2015, Classical and quantum gravity, 32, 074001
- Abadi, M., Agarwal, A., Barham, P., et al. 2015, TensorFlow: Large-Scale Machine Learning on Heterogeneous Systems. <https://www.tensorflow.org/>
- Abbott, B. P., Abbott, R., Abbott, T., et al. 2020, Living reviews in relativity, 23, 1
- Boyle, M., Hemberger, D., Iozzo, D. A., et al. 2019, Classical and Quantum Gravity, 36, 195006
- Cotesta, R., Marsat, S., & Pürrer, M. 2020, Physical Review D, 101, 124040
- Edwards, T. D. P., Wong, K. W. K., Lam, K. K. H., et al. 2023, RIPPLe: Differentiable and Hardware-Accelerated Waveforms for Gravitational Wave Data Analysis. <https://github.com/tedwards2412/ripple>
- García-Quirós, C., Colleoni, M., Husa, S., et al. 2020, Phys. Rev. D, 102, 064002, doi: [10.1103/PhysRevD.102.064002](https://doi.org/10.1103/PhysRevD.102.064002)
- Hannam, M., Schmidt, P., Bohé, A., et al. 2014, Physical review letters, 113, 151101
- Husa, S., Khan, S., Hannam, M., et al. 2016, Physical Review D, 93, 044006
- Islam, T., Field, S. E., Hughes, S. A., et al. 2022, Physical Review D, 106, 104025
- Khan, S., Husa, S., Hannam, M., et al. 2016, Physical Review D, 93, 044007
- Ossokine, S., Buonanno, A., Marsat, S., et al. 2020, Physical Review D, 102, 044055
- Paszke, A., Gross, S., Massa, F., et al. 2019, in Advances in Neural Information Processing Systems 32, ed. H. Wallach, H. Larochelle, A. Beygelzimer, F. d'Alché-Buc, E. Fox, & R. Garnett (Curran Associates, Inc.), 8024–8035. <http://arxiv.org/abs/1912.01703>

Pratten, G., Husa, S., Garcia-Quiros, C., et al. 2020,  
Physical Review D, 102, 064001

Pratten, G., García-Quirós, C., Colleoni, M., et al. 2021,  
Physical Review D, 103, 104056

Pürrer, M., & Haster, C.-J. 2020, Physical Review  
Research, 2, 023151

Taracchini, A., Buonanno, A., Pan, Y., et al. 2014, Physical  
Review D, 89, 061502

Varma, V., Field, S. E., Scheel, M. A., et al. 2019a,  
Physical Review Research, 1, 033015

—. 2019b, Physical Review D, 99, 064045